Regenerative Engineering and Translational Medicine (2018) 4:257–267
https://doi.org/10.1007/s40883-018-0067-x

Fabrication of a Free Radical Scavenging Nanocomposite Scaffold for Bone Tissue Regeneration

Krista Dulany[1] · Allison Goins[1] · Adam Kelley[2] · Josephine B Allen[1]

Received: 9 April 2018 / Accepted: 15 June 2018 / Published online: 29 June 2018

Abstract

Oxidative stresses have become a large influence on bone tissue regeneration. Increased by trauma and fracture, reactive oxygen species (ROS) negatively impact the remodeling function of osteoblasts by damaging DNA and cellular structures while triggering apoptosis. This greatly hinders the efficacy of bone grafts to facilitate bone remodeling. Cerium oxide nanoparticles (CNPs) have been utilized to reduce ROS and have made an impact in biological applications. In this study, we fabricated bioactive, nanocomposite scaffolds incorporating cerium oxide nanoparticles. The architectural, chemical, and mechanical properties of the scaffolds were characterized using techniques such as scanning electron microscopy, energy-dispersive X-ray spectroscopy, X-ray diffraction, and compression testing. Biological assessments were completed to gauge the pro-osteogenic nature of the scaffolds through the attachment, viability, and mineralization of a pre-osteoblast cell line. Finally, free radical scavenging (FRS) function of the scaffolds was tested by measuring the decomposition of hydrogen peroxide over time and quantifying the cytotoxicity of cells on scaffolds after inducing oxidative stress. Through these assessments, it was determined that the nanocomposites contained the desired porous architectural and chemical properties. Scaffolds exhibited biocompatibility by supporting cell attachment, viability, and initiation of mineralization in the absence of supplemental mineralization-promoting factors. FRS behavior was displayed via a statistically significant reduction in scaffold-mediated hydrogen peroxide concentration and functional protection of cells from induced oxidative stress. In this work, we show that the successful incorporation of CNPs into nanocomposite scaffolds was able to decrease free radical damage to cells while providing a suitable environment for pre-osteoblast cells.

Lay Summary

The function of bone-forming cells, osteoblasts, in the bone remodeling cycle is hindered by oxidative stress created by an increase of reactive oxygen species. This is often seen at sites of injury and surgery, where bone grafts are often utilized. Our group investigated incorporating cerium oxide nanoparticles into a bioactive polymer-ceramic nanocomposite scaffolds for bone grafting applications. By incorporating the nanoparticles into our system, we are able to create a bioactive scaffold that can reduce reactive oxygen species and support osteogenic cell growth, both requirements for bone tissue formation. After initial in vitro testing, we would like to expand our investigation of the nanocomposite system in various in vivo models. To begin, an ectopic study in mice to determine biocompatibility, immune response, and mineralization. Additional studies would follow including critical size defect models in larger animal models.

Keywords Free radical scavenging · Cerium oxide nanoparticles · Nanocomposite scaffolds · Bone tissue regeneration

Introduction

Globally, an estimated 15 million bone fracture cases are reported per year and nearly 600,000 bone grafting procedures are completed [1, 2]. Autologous tissue grafts are currently the gold standard to support bone regeneration due to high compatibility, reduced rejection, and increased osteoconductive and osteoinductive properties [1, 3]. While these grafts are ideal, they are not without their challenges; common

✉ Josephine B Allen
jallen@mse.ufl.edu

[1] Department of Materials Science and Engineering, University of Florida, 100 Rhines Hall, Gainesville, FL 32611, USA

[2] Department of Mechanical and Aerospace Engineering, University of Florida, 300 Weil Hall, Gainesville, FL 32611, USA

complications include donor site morbidity, resource limitations, and incomplete graft incorporation [1, 3]. Allogeneic grafts provide an abundant alternative to autologous tissues; however, this approach can result in disease and pathogen transmission as well as graft rejection by the host immune system [1, 3]. Collectively, these challenges have led to the use of synthetic materials for bone scaffold fabrication; however, these often promote lower levels of osteoconductivity, vascularization, and osseointegration [1, 4, 5]. These limitations have motivated the field of bone tissue engineering to develop bioactive systems to promote tissue restoration and address biological conditions present at the fracture site.

The increased presence of reactive oxygen species (ROS) at bone fracture sites is a biological condition limiting bone regeneration at grafting locations. Fracture and cutting from surgery are major sources of free radicals in the bone due to the stress the tissue is put under [6]. High levels of ROS can damage cellular structures through lipid and protein oxidations, alterations to the integrity of mitochondrial and nuclear DNA, or apoptosis and necrosis of osteoblastic cells [7, 8]. It has been found that high levels of oxidative stress not only damage cell integrity but also deter the natural bone remodeling cycle by inhibiting osteoblastic differentiation and remodeling function. Oxidative stress boosts osteoclast behavior, increasing bone resorption resulting in decreased bone mineral density [7, 9]. This particular challenge is typically not considered when designing a bone scaffold but is gaining interest as free radical scavenging agents are being utilized.

One such agent, cerium oxide nanoparticles (CNPs) have become an interest in tissue engineering because of their free radical scavenging (FRS) potential [8, 10–15]. Research has shown that CNPs increase cellular viability and proliferation by reducing local free radicals [8, 16–18]. CNPs have a cubic fluorite structure with mixed vacancy states of Ce^{3+} and Ce^{4+} at surface oxygen sites that host redox reactions using multiple reaction paths [8, 10, 19]. Due to their high surface area to volume ratio, nanoparticles are preferred because they have the most surface active sites in comparison to larger particles [12]. It has been shown that CNPs behave as synthetic superoxide dismutase (SOD) and catalase enzyme mimetics, reducing free radicals [20–22]. Recently, their properties have been investigated in biological applications that include acting as anti-radiation, anti-inflammatory, and antioxidant agents for the treatment of retinal damage, cardiovascular pathologies, and neurodegenerative disorders [8, 10, 11, 13, 18, 23]. These unique properties have led our group to investigate the FRS abilities of CNPs when incorporated into a traditional nanocomposite system that shows great promise for bone tissue engineering.

Common material approaches to engineer synthetic bone grafts include the use of both natural and synthetic biocompatible polymers, such as collagen, polylactic acid (PLA), polycaprolactone (PCL), and poly diol citrates (PDC) [3, 4, 24, 25]. As bone graft materials, these materials are less than ideal alone as they do not have inherent osteoconductive behavior [3, 4]. To achieve the requisite bone-specific properties, calcium phosphates are often added to scaffolds to provide mechanical support to polymeric matrices [26–28]. The addition of calcium phosphates also contributes to increasing the bioactive properties of the scaffolds, such as cell adhesion and the ability of the scaffold to interface with the adjacent bone through direct biochemical bonds [26–28]. Common calcium phosphates used in bone regeneration are hydroxyapatite (HA) and β-tricalcium phosphate (β-TCP), a faster degrading synthetic alternative to hydroxyapatite (HA) [4, 29, 30]. Common scaffold architectures for bone substitutes and fillers include cements, pastes, and foams constructed of polymers, ceramics, and composites of both [1]. Fabrication methods to create these scaffolds include gas foaming, solvent casting and particle leaching, solid free-form printing, electrospinning, and freeze casting to create porous structures that have the ability to host bone regeneration [4, 5, 31]. Using a particulate leaching method, our research group previously designed and successfully fabricated a nanocomposite scaffold composed of a PDC matrix and β-TCP filler [3]. This system serves as a foundation for our exploration into bone tissue regeneration. Synthetic scaffolds can be fabricated on demand, customized to the needs of the patient, and optimized to deliver drugs and growth factors to recruit cells to repair damaged tissue [1, 29, 32].

This study investigates the fabrication and characterization of a free radical scavenging nanocomposite scaffold to repair and regenerate defects in the bone. The composite is fabricated using a particulate leaching method to create a porous scaffold composed of 1,8 poly(octanediol-co-citrate) (POC), a biocompatible, biodegradable elastomer; β-TCP, a bioactive calcium phosphate ceramic; and CNPs, a free radical scavenging agent. The scaffold's physical and chemical properties are quantified. The scaffolds are then assessed for biocompatibility using a pre-osteoblast cell line, followed by measuring inherent free radical scavenging abilities through assays quantifying the reduction in hydrogen peroxide concentration as well as the effects of induced oxidative stress on cellular viability.

Materials and Methods

Materials

Poly (1,8 octanediol-co-citrate) (POC) precursors, 1,8 octanediol, and citric acid were purchased from Sigma-Aldrich, St. Louis, MO. Medical-grade β-tricalcium phosphate (β-TCP) nanoparticles, 100 nm in diameter, were purchased from Berkeley Advanced Biomaterials, San Leandro, CA. Cerium oxide nanoparticles (CNPs), < 25 nm in diameter,

and sodium chloride (salt) were also both purchased from Sigma-Aldrich, St. Louis, MO.

Scaffold Fabrication

Synthesis of poly(1,8 octanediol-co-citrate) (POC) was conducted as previously described [33]. Briefly, 1,8 octanediol and citric acid were heated under stirring at 160 °C until molten. The temperature was lowered to 140 °C and held for approximately 1 h to allow the polycondensation of the 1,8 octanediol and citric acid. The reaction is then quenched, the pre-polymer is dissolved in ethanol, and then purified in water. The purified pre-polymer is lyophilized and dissolved in ethanol to create a 30 wt.% pre-polymer solution.

The composite scaffold was fabricated with 65 wt.% POC pre-polymer and 35 wt.% blend of β-TCP and CNPs. CNPs were incorporated at ratios of 10 and 20 wt.% relative to POC. Scaffolds containing POC and only β-TCP without CNPs are referred to as PT, and POC and β-TCP scaffolds containing 10 and 20% CNPs are referred to as PTC10 and PTC20, respectively. To render the scaffolds 80% porous, we utilized a particulate leaching method as previously described [3]. Briefly, salt was sieved to 250–300 μm and blended with POC pre-polymer and β-TCP via physical mixing in a Teflon dish. To evaporate the ethanol, the mixture was repeatedly placed into an 80 °C oven for 5, 2, and 1 min(s) with mixing between steps. CNPs were then blended via physical mixing into the system. The mixture was then tightly packed into a Teflon dish and thermally crosslinked for 3 days at 80 °C. After crosslinking, the scaffold was carefully removed from the Teflon dish and placed in deionized water to remove the salt and create the porous network. The scaffolds were then air-dried and prepared for various assays. In all assays, unless stated otherwise, scaffolds were bored to create small cylindrical samples. The scaffolds were measured to be approximately 3 mm in diameter and 3 mm in height, resulting in a volume of ~ 85 mm^2.

Scaffold Characterization

Scanning Electron Microscopy

Sample cross-sections were imaged using scanning electron microscopy (SEM) to qualitatively examine pore morphology and surface topography. Samples were prepared for scanning electron microscopy by mounting onto microscopy stubs and coating with gold-palladium or carbon to reduce sample charging. Samples were imaged using a PhenomWorld ProX desktop electron microscope (PhenomWorld, Eindhoven, Netherlands) at a beam energy of 15 kV. Pore size was measured from scanning electron micrographs taken of various cross-sections of scaffolds that had been hydrated and dehydrated using the ImageJ software provided by the National Institutes of Health. Five random pores in each quadrant of the micrograph were measured in two dimensions across five micrographs of a given sample type. Measurements were then averaged, and a pore size distribution was created.

Mechanical Properties

Compressive mechanical properties were measured using an Instron 5943 (Norwood, MA) equipped with a 10-kN compressive load cell and an anvil extension. Samples were assessed in accordance with ASTM D695-15. A total of eight samples ($n = 8$) were tested for each scaffold type. All samples contained a dimension ratio of sample height equal to twice the diameter, 6 to 3 mm. A crosshead speed of 1.0 mm/min was used to measure the compressive properties. Samples were hydrated in deionized water for 20 min prior to testing and blotted dry using a KimWipe. Young's modulus values were calculated by identifying the linear elastic region of the scaffolds and determining the slope of the stress-strain curves.

Energy-Dispersive X-ray Spectroscopy

Energy-dispersive X-ray spectroscopy (EDS) was completed to qualitatively identify elements present at the surface of the scaffold walls, specifically calcium, phosphorus, and cerium. Samples were mounted on microscopy stubs and coated with a thin layer of carbon to reduce charging. Samples were analyzed using a PhenomWorld ProX (PhenomWorld) system containing CeB_6 electron source and a silicon drift detector (SDD) type. This was completed at a beam energy of 15 kV.

X-ray Diffraction

The presence of β-TCP and the CNPs throughout the scaffold was assessed using an X-ray powder diffractometer (AXRD Benchtop X-Ray Powder Diffractometer, PROTO Manufacturing Inc., Taylor, Michigan). The nanocomposite scaffolds were loaded into the machine, under the exposure of Cu-K_α X-rays. A diffraction range of 20–100° was scanned with a step size of 0.2°. The resulting diffraction patterns from POC only scaffolds, PT, PTC10, and PTC20 were compared for the presence of peaks at characteristic 2 locations for β-TCP and CNP. The background eliminated spectra were plotted for all samples. Spectra were validated using the Inorganic Crystal Structure Database (ICSD) reference cards.

Biocompatibility and Cell Behavior Assessments

Cell Culture

MC3T3-E1 mouse calvaria pre-osteoblast subclone-4 ATCC CRL-2593 (ATCC, Manassas, VA) was used to assess

scaffold cellular compatibility and functionality. Cells were cultured in Alpha Minimum Essential Medium (αMEM) without ascorbic acid (Gibco, Carlsbad, CA) supplemented with 10% heat-inactivated fetal bovine serum (Corning, Corning, NY), 1% penicillin-streptomycin (Corning, Corning, NY), and 0.2% fungizone (Gibco, Carlsbad, CA). MC3T3 cells were cultured in a humidified atmosphere, 5% CO_2 at 37°C. Media was changed every 2–3 days. Scaffolds were sterilized via ethylene oxide gas (Anprolene AN74i, Haw River, NC) for 12 h.

Cell Attachment

To study cell attachment, MC3T3 cells were seeded onto nanocomposite scaffolds, ~ 85 mm^2, at a density of 20,000 cells per scaffold in a 24-well ultra-low attachment plate (Corning, Corning, NY) and incubated for 7 days in complete αMEM. Scaffolds were then rinsed with phosphate-buffered saline (PBS) (Corning, Corning, NY) to remove excess media, fixed in a 2.5% (*v*/*v*) glutaraldehyde solution for 30 min at 4 °C, and washed three times with deionized water to remove residual glutaraldehyde. The scaffolds were then serially dehydrated in ethanol, lyophilized overnight (Labconco, Kansas City, MO), mounted onto SEM stubs, coated with gold-palladium, and imaged using SEM.

Cell Viability

A colorimetric lactate dehydrogenase (LDH) cytotoxicity assay kit (Thermo Scientific Pierce, Waltham, MA) was used to quantify the amount of LDH released by damaged or distressed MC3T3 cells. Cells were seeded onto scaffolds ~ 85 mm^2 at 15,000 cells per scaffold ($n = 4$) in a 24-well ultra-low attachment plate (Corning) and grown in complete αMEM media. Media supernatant was assayed for soluble LDH concentration in accordance with the LDH kit manufacturer's protocol after 7 days of incubation. The sample aliquots were read in triplicate at 490 and 680 nm using a Synergy H1 spectrophotometer (BioTek, Winooski, VT).

Mineralization

Mineralization by MC3T3 cells grown on PT, PTC10, and PTC20 scaffolds was measured quantitatively using alizarin red stain. MC3T3 cells were seeded onto each scaffold, ~ 85 mm^2, ($n = 5$) at 50,000 cells per scaffolds. MC3T3 cells were grown in complete media for 10 days to assess mineral production and deposition. To prepare the cell-seeded scaffolds for staining, the scaffolds were gently washed with PBS and fixed with 2.5% (*v*/*v*) glutaraldehyde for 30 min at 4 °C. The scaffolds were then washed with deionized water to remove residual fixative and stained with 1 mL of 2% Alizarin Red Stain (Poly Scientific R&D, Bay Shore, NY) for 30 min at room temperature. Deionized water washes were then used to remove excess stain. Alizarin red was quantified using 500 μL of 10% (*w*/*v*) cetylpyridinium chloride to release the calcium-bound stain. Samples were read in duplicate 100 μL aliquots at 550 nm using a Synergy H1 Spectrophotometer.

Free Radical Scavenging Functionality

Hydrogen Peroxide Decomposition

The degradation of hydrogen peroxide, when exposed to the nanocomposite scaffolds, was measured using a colorimetric Pierce Quantitative Peroxide Assay Kit (Thermo Scientific Pierce, Waltham, MA). Scaffolds, ~ 85 mm^2, ($n = 6$) were immersed in 1 mL of a 100-μM hydrogen peroxide solution in water for 7 days. Samples were wrapped in foil to reduce light exposure and placed in a 37 °C incubator to simulate body temperature. The concentration of hydrogen peroxide was measured at time points of 1 h, 1, 4, and 7 days in accordance with kit procedure. Absorbance was measured at 595 nm using a Synergy H1 Spectrophotometer.

Cell Viability Under Oxidative Stress

A colorimetric lactate dehydrogenase (LDH) cytotoxicity assay kit was modified to quantify the amount of LDH released by cells that are damaged when exposed to a simulated peroxide source. MC3T3 cells were seeded in αMEM onto nanocomposite scaffolds, ~ 85 mm^2, at 20,000 cells per scaffold in a 24-well ultra-low attachment plate (Corning) in complete αMEM media and allowed to attach and recover over 2 days. The media was then changed to either (1) complete αMEM media, (2) αMEM containing 1 mM H_2O_2, or (3) complete αMEM with the addition of the kit provided 10× lysis buffer to represent maximum cytotoxicity. The nanocomposite scaffolds ($n = 5$) were incubated for 2 h and the media was then assayed for LDH concentration in accordance with the kit protocol. Absorbance was read at 490 and 680 nm using a Synergy H1 spectrophotometer.

Statistical Analysis

All numerical data will be reported as the mean ± standard deviation. Outliers were determined using the ROUT method with ($Q = 1\%$). Statistical significance was assessed using a one-way and two-way analysis of variance test (ANOVA) with a Tukey's multiple comparisons post hoc analysis. All samples had an $\alpha = 0.05$ and a p value < 0.05 was used to confirm statistical significance.

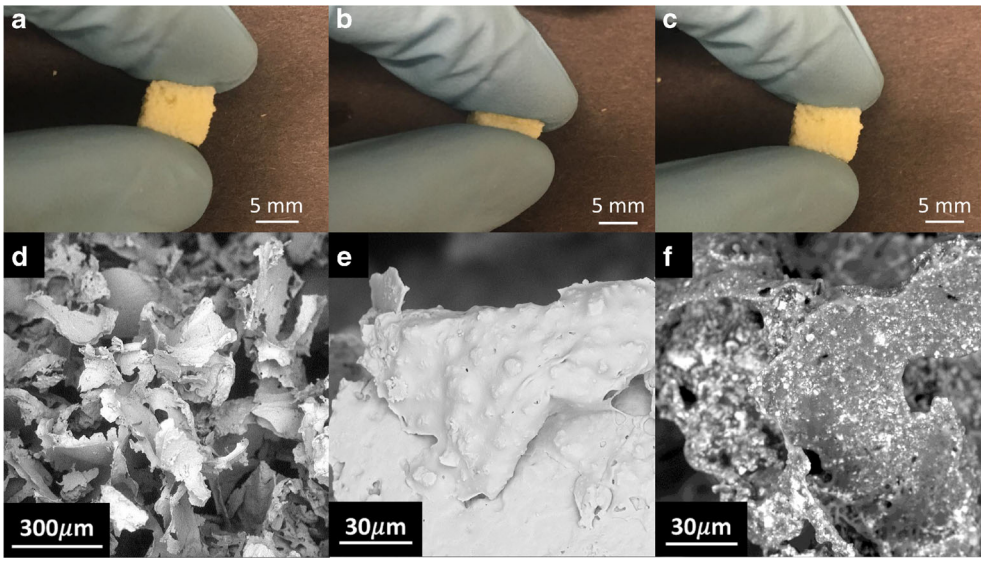

Fig. 1 Representative images of nanocomposite constructs. **a**–**c** Digital images of PTC20 scaffolds undergoing compression and recovery. Scanning electron micrographs of PTC20 nanocomposite scaffolds, focusing on **d** pore morphology, **e** surface topography, and **f** compositional contrast of the pore walls

Results

Scaffold Characterization

Scanning Electron Microscopy

Nanocomposite scaffolds resembling sponges that are easy to handle, shape, and recover under compressive forces were fabricated (Fig. 1a–c). The nanocomposites were observed under SEM and confirm the expected interconnected porous network that was created from salt particle leaching (Fig. 1d). SEM images revealed surface topography that could be associated with the nanoparticle components (Fig. 1e). The compositional contrast of the scaffold materials in the pore walls was imaged and qualitatively assessed (Fig. 1f). From the contrast, it was shown that the particles were incorporated throughout the pore walls and not in segmented clusters. Pore size was determined by measuring pores in micrographs such as these. It was determined that the average pore size of dehydrated scaffolds was 222.7 ± 48.7 μm across all nanocomposite scaffold compositions.

Mechanical Properties

Mechanical testing was done to quantify Young's modulus for each of the nanocomposite scaffolds in compression ($n = 8$) (Fig. 2a, b). To quantify Young's moduli, the slope of the stress-strain diagrams was taken between strain values around 0.6–0.75 (mm/mm), as seen in the magnified graph in Fig. 2a. After analysis, it was found that PT, PTC10, and PTC20 scaffolds contained average Young's moduli measuring 1.24 ± 0.28, 1.18 ± 0.15 MPa, and 1.26 ± 0.30 MPa, respectively. A one-way ANOVA analysis with a Tukey multiple comparison post hoc analysis was used to compare average Young's moduli between the scaffold types. There were no significant differences in the mechanical properties of each sample type ($\alpha = 0.05$, $p = 0.8352$).

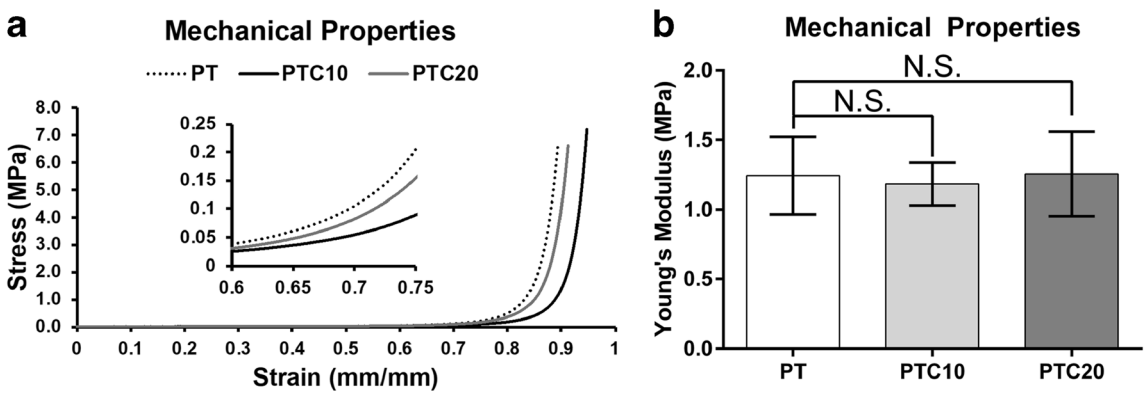

Fig. 2 Compressive mechanical properties assessment. **a** Stress-strain of PT, PTC10, and PTC20 scaffolds in compression and **b** average Young's moduli ($n = 8$) of nanocomposite scaffolds. Results are reported as mean ± standard deviation. No statistically significant difference between comparison groups is denoted with N.S.

Energy-Dispersive X-ray Spectroscopy

EDS spectra of characteristic X-rays were collected to confirm the presence of β-TCP and CNPs at the surface of the scaffold pore walls. High counts of X-rays were identified at 4.8 and 5.2 keV, both characteristic to the element cerium (Fig. 3a–c). The identification of the element cerium implies the presence of cerium oxide at the surface. Other elements identified in the spectra were indicative of the β-TCP used in fabrication. High counts of carbon were identified due to the conductive carbon coating on the scaffold.

X-ray Diffraction

The presence of β-TCP and CNPs in the scaffolds was confirmed by X-ray diffraction (XRD). A sample background was collected with the nanocomposite scaffold composed of POC only (Fig. 3d). The spectra obtained for the PT scaffold had the characteristic peaks for β-TCP (denoted by triangles) around 2 (lattice plane) values of 26° (1010), 28° (214), 31° (0210), 35° (220), and 53° (2020) [34]. The spectra that were obtained for PTC10 and PTC20 samples containing both β-TCP and CNPs had the peaks characteristic of β-TCP, as well as CNPs (denoted by circles) at 2 values of 29° (111), 33° (200), 48° (220), 58° (311), 59° (222), 65° (400), 77° (331), 79° (420), and 88° (422) [35]. XRD spectra for the PTC samples confirmed the presence of the β-TCP (ICSD 98-000-0923) and CNPs (ICSD 98-015-5604). Of note, there was a reduction in the intensity of the β-TCP peaks in the PTC samples which were expected as the concentration of β-TCP was decreased to accommodate the CNPs. Additionally, the intensity of the CNP peaks was greater in the PTC20 sample than the PTC10.

Biocompatibility Assessment

Cell Attachment

Nanocomposite scaffolds seeded with MC3T3 cells were imaged using scanning electron microscopy to visualize cell attachment to the surface of the nanocomposite scaffolds. Imaging revealed MC3T3 attachment to the surface of PTC20 scaffolds, highlighted by arrows (Fig. 4a, b). Cell attachment on PTC20 scaffolds was representative of the attachment of MC3T3 cells on both PT and PTC10 scaffolds. The cells are round figures with small appendages bridging out from the center. In these micrographs, there is an abundance of cells attached to each scaffold type. This cell attachment demonstrates that the scaffolds are biocompatible and support the attachment of MC3T3 pre-osteoblasts.

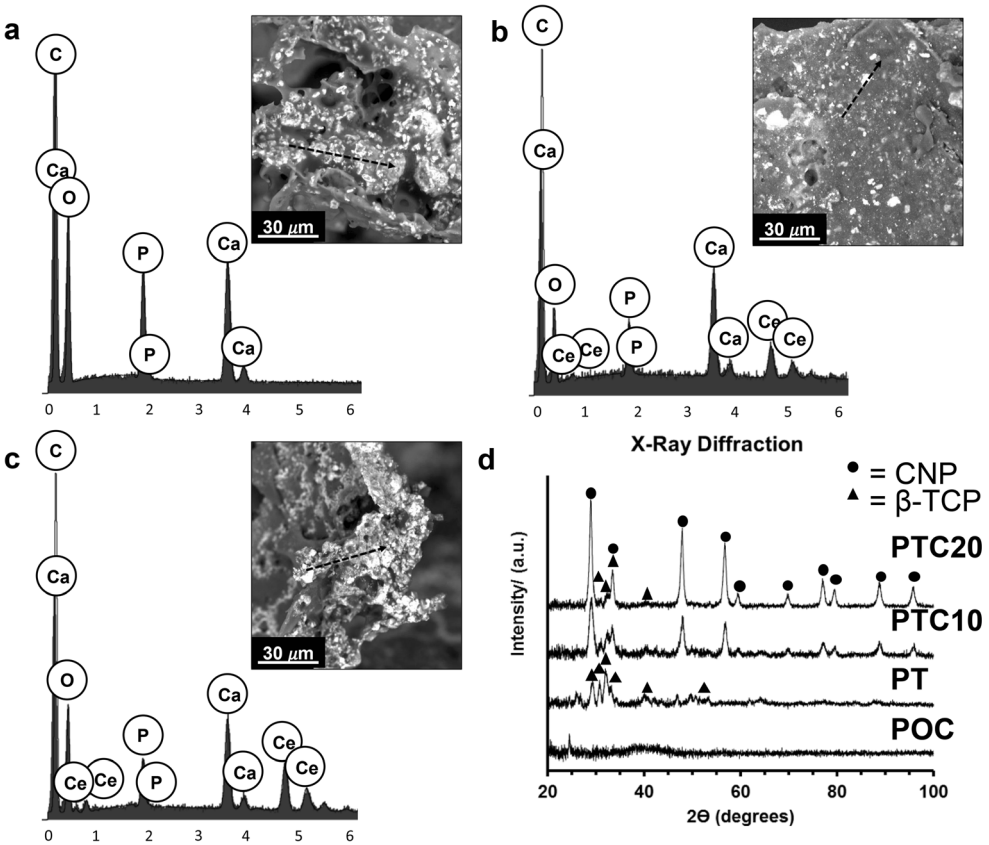

Fig. 3 Chemical analysis of nanocomposite scaffolds. **a–c** Representative EDS spectra of PT, PTC10, and PTC20 samples. **d** XRD of POC, PT, PTC10, and PTC20 scaffolds

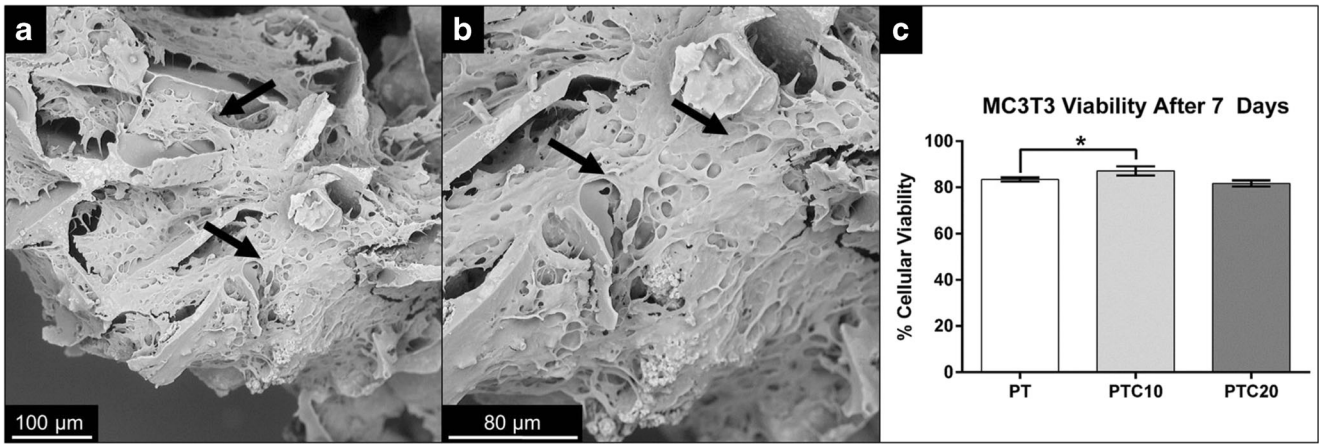

Fig. 4 Scanning electron micrographs of MC3T3 pre-osteoblast cells attached (highlighted by arrows) to the surface of a PTC20 scaffold (**a**, **b**). Cell attachment on PTC20 scaffolds is representative of attachment on both PT and PTC10 scaffold surfaces. **c** Viability of MC3T3 cells on scaffolds ($n = 4$) measured after 7 days of culture. Average viability was reported as mean ± standard deviation; statistically significant change is denoted by the * symbol

Cell Viability

The viability of MC3T3 cells was determined through colorimetric quantification of the intracellular enzyme LDH which, when released into culture media is indicative of cellular damage (Fig. 4c). To calculate percent viability, a maximum LDH value was collected from MC3T3 cells cultured on each scaffold type, PT, PTC10, and PTC20, by exposing the cells to a lysis buffer provided by the kit. The LDH values from cells normally seeded on scaffolds were then divided by the maximum to generate a percent cytotoxicity, which can then be transformed into percent viability by subtracting from 100%. The relative percentages of MC3T3 cellular viability at day 7 in culture on PT, PTC10, and PTC20 ($n = 4$) scaffolds were determined to be 83.42 ± 0.90, 87.10 ± 1.98, and 81.68 ± 1.29%, respectively. Using a one-way ANOVA and Tukey's multiple comparisons test, it was determined that there was a significant increase in cellular viability between PT and PTC10 scaffolds ($\alpha = 0.05$, $p = 0.0003$) and no significant differences were determined between PT and PTC20 scaffolds. All levels of cell viability were above 80% indicating low amounts of cytotoxicity.

Mineralization

Mineralization by MC3T3 cells cultured on PT, PTC10, and PTC20 scaffolds was determined by quantifying alizarin red stain using cetylpyridinium chloride to solubilize calcium-bound stain (Fig. 5). After 10 days of culture on the scaffolds ($n = 5$), the average optical density of alizarin red stain obtained from PT, PTC10, and PTC20 scaffolds was determined to be 0.054 ± 0.024, 0.033 ± 0.016, and 0.016 ± 0.004, respectively. Outliers in PTC20 scaffolds were identified and removed using the ROUT method ($Q = 1\%$). Using a one-way ANOVA and Tukey's multiple comparisons test, it was determined that there were significant differences in mineralization between PT scaffolds devoid of cerium oxide nanoparticles and PTC10 and PTC20 scaffolds ($\alpha = 0.05$, $p = 0.0005$). The average decrease in mineralization across the scaffolds can be attributed to the corresponding decrease in β-TCP across the scaffold compositions due to the inclusion of CNPs within PTC10 and PTC20 scaffolds.

Free Radical Scavenging Functionality

Hydrogen Peroxide Decomposition

In the absence of any cellular component, the nanocomposite scaffold's inherent ability to decompose hydrogen peroxide to water was measured over the course of 7 days (Fig. 6a). Scaffolds ($n = 6$) were exposed to a 100-μM concentration of hydrogen peroxide in water, and after 1 h and 1, 4, and 7 days, the concentration of H_2O_2 still in solution was measured. To quantify the H_2O_2, a colorimetric assay was used to convert remaining hydrogen peroxide in solution to a purple color with

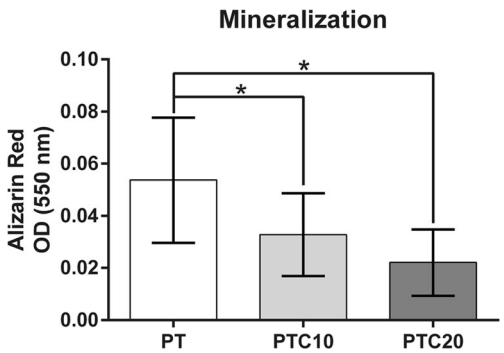

Fig. 5 Quantification of Alizarin Red stain to determine mineralization by MC3T3s cultured on PT, PTC10, and PTC20 scaffolds ($n = 5$) for 10 days. Average OD from alizarin red stain was reported as mean ± standard deviation; statistically significant change is denoted by the * symbol

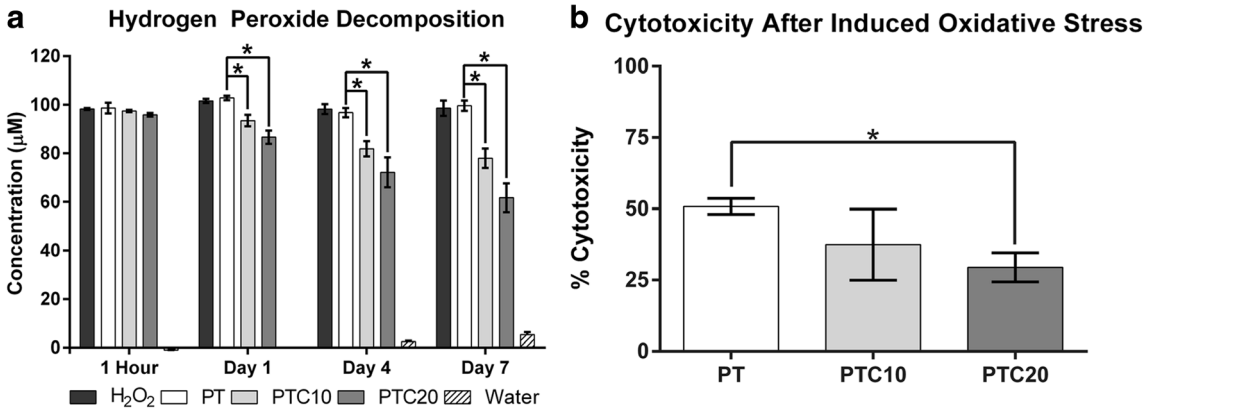

Fig. 6 Assessment of free radical scavenging behavior of the nanocomposite scaffolds. **a** Quantifying free radical scavenging behavior by measuring hydrogen peroxide decomposition in water after scaffold exposure over 7 days ($n = 6$). **b** Assessment of FRS behavior in an in vitro model, inducing oxidative stress on MC3T3s seeded onto scaffolds ($n = 5$). Average concentration and cytotoxicity were reported as mean ± standard deviation; statistically significant change is denoted by the * symbol

varied intensity based on the amount of H_2O_2 present. Our data show that at the time points tested, the concentrations of H_2O_2 remaining in solution after exposure to the nanocomposite scaffolds PT, PTC10, and PTC20 were (1 h 98.70 ± 2.20 μM, day 1 102.90 ± 0.90 μM, day 4 96.79 ± 1.92 μM, and day 7 99.64 ± 2.11 μM.), (1 h 97.45 ± 0.51 μM, day 1 93.54 ± 2.37 μM, day 4 81.85 ± 3.14 μM, and day 7 77.98 ± 3.97 μM.), and (1 h 95.91 ± 0.74μM, day 1 86.66 ± 2.76 μM, day 4 72.17 ± 6.12 μM, and day 7 61.71 ± 5.89 μM), respectively. As a reference for spontaneous degradation, we quantified the H_2O_2 in solution with no exposure to scaffolds and found that the concentration did not experience significant change over time (1 h 98.31 ± 0.40 μM, day 1 101.60 ± 0.82 μM, day 4 98.25 ± 2.02 μM, and day 7 98.63 ± 3.16 μM). A two-way ANOVA with a Tukey's multiple comparison post hoc test was used to compare scaffolds to each other at each time point as well as compare changes in concentrations over time within each scaffold type. These data show that in comparison to PT (POC—β-TCP only) scaffolds, the scaffolds with incorporated CNPs, PTC10 and PTC20, experienced significant decreases in H_2O_2 concentration at each time point ($\alpha = 0.05$, $p < 0.0001$). There was no significant difference between H_2O_2 concentrations of PT scaffolds and spontaneous decomposition, confirming that CNPs caused the decrease in peroxide concentration.

Cell Viability Under Oxidative Stress

An LDH cytotoxicity assay was used to determine the percent cytotoxicity of MC3T3 cells on nanocomposite scaffolds after acute exposure to a 1-mM hydrogen peroxide media solution (Fig. 6b). Percent cytotoxicity was calculated by dividing the signal created from H_2O_2-induced cytotoxicity by the maximum cytotoxicity created by lysis buffer exposure. The cytotoxicity of MC3T3 cells on PT, PTC10, and PTC20 scaffolds was determined to be 50.83 ± 2.81, 37.44 ± 12.47, and 29.43 ± 5.07%, respectively. Outliers in PT and PTC20 scaffolds were identified and removed in accordance with a ROUT ($Q = 1\%$) analysis. After analysis using a one-way ANOVA and Tukey's multiple comparisons test, to compare cytotoxicity values between each scaffold type, it was determined that PTC20 scaffolds had significantly lower cytotoxicity values in comparison to PT scaffolds, ($\alpha = 0.05$, $p < 0.0001$).

Discussion

Various material combinations and fabrication methods have been used to form osteoconductive bone nanocomposites for tissue regeneration [36]. Increased free radical species at sites of fracture and surgery remain a challenge to bone tissue grafting and regeneration. Free radicals place cells in a state of oxidative stress; which can reduce osteoblastic differentiation, hindering remodeling and regeneration of the bone while in turn also increasing osteoclastic bone resorption [7, 37]. In an attempt to combat the problems associated with increased ROS, we looked toward incorporating the free radical scavenging agent, cerium oxide nanoparticles, into a POC polymer and β-TCP ceramic nanocomposite system. Work completed by Karakoti et al., Mandoli et al., and Li et al. found that CNPs exhibit FRS behavior when free in solution, incorporated in poly(lactic-co-glycolic acid) (PLGA) and ceramic coatings, respectively [8, 10, 38]. These findings support the investigation into the incorporation of CNPs in nanocomposite systems for bone regeneration.

The particle leaching method was chosen to fabricate flexible nanocomposites with a porous, sponge-like structure resembling scaffolds produced in previous studies by Baler et al. [3]. In a review of functionally graded tissue engineering scaffolds, Leong et al. determined that pores ranging from 100 to 300 μm are preferred by bone cells [30]. Utilizing this fabrication method allowed for discretization of pore size between 250 and 300 μm. Using SEM, a qualitative assessment of scaffold

topography and composition distribution was completed. To quantify the specific contribution of β-TCP and CNPs to surface topography, further characterization would be required. However, rough surface topography of cell interfacing surfaces, especially by bioactive materials such as β-TCP, has shown increased levels of cell attachment [1, 39]. It was important to confirm the localization of β-TCP and CNPs on the cell-contacting surfaces because (1) calcium phosphates are osteoconductive and have been shown to direct bone-type cells down osteogenic pathways and (2) CNPs partake in free radical scavenging behavior to reduce levels oxidative stress [1, 39]. The mechanical properties of our scaffolds were investigated to ensure that the addition of CNPs would not affect the integrity of the composite. Through compression testing, it was confirmed that there was no significant difference in Young's moduli between scaffolds with and without CNPs. We hypothesize that this is a result of the equal replacement of a fraction of the β-TCP by the CNPs.

To confirm the presence of the CNPs, EDS and XRD were used to assess the composition of the scaffolds. EDS was used to identify characteristic X-rays of elements present at the scaffold surface. In this case, cerium was identified along with oxygen and phosphorous confirming the presence of β-TCP and CNPs. XRD was used as an additional method to identify β-TCP and CNPs throughout the nanocomposites to confirm distribution of the nanoparticles. It is important to note that through this method, the changes in scaffold composition were reflected in the spectra. POC scaffolds contained no identifiable peaks, while PT scaffolds contained characteristic peaks for β-TCP only. Spectra obtained from PTC10 and PTC20 scaffolds displayed peaks for β-TCP and CNPs. The transition in composition across the scaffolds was seen in the decrease of β-TCP and increase in CNP peak intensity. The identification of the particles was of particular importance, because without the CNPs at the surface or throughout the scaffold, there would be no free radical scavenging behavior.

A biocompatibility assessment was completed using an MC3T3 pre-osteoblast cell line. After 7 days, cell attachment was evident in all three scaffold types, PT, PTC10, and PTC20. MC3T3 cells can be seen throughout the porous networks, branching across the scaffold surface like on the PTC20 scaffolds imaged. This confirmed that the scaffold compositions were able to host pre-osteoblast cell attachment and growth. Cellular viability was assessed by quantifying LDH release after 7 days. It was determined that all three of the nanocomposite structures were non-cytotoxic and biocompatible containing cellular viabilities above 80%. Our internal controls of cells grown on tissue culture polystyrene (not graphed) showed normal cell viability to be 87.38 ± 1.50%. Therefore, the cells cultured on the nanocomposite scaffolds are within the range of normal cell turnover. Therefore, we conclude that the incorporation of CNPs into the scaffolds did not affect cellular viability, conclusive to the findings of Karakoti et al. who reported that CNP contact is non-toxic to cells [17]. It was discovered that all three scaffold variants initiated mineralization in complete media, without osteogenic supplements, beta-glycerophosphate, or ascorbic acid. The degree of mineralization decreases across the three scaffold types, PT, PTC10, and PTC20, which contain 0, 10, and 20% CNPs respectively. The decrease in mineralization is hypothesized to be a result of the decreasing amount of β-TCP that accompanies the increasing concentration of CNP in the PTC10 and PTC20. This interesting observation of the tradeoff in scaffold properties between mineralization and free radical scavenging may be dependent on the ratio of β-TCP and CNPs. Further investigation of this tradeoff is required for the development of a more tunable design.

The nanocomposite's inherent ability to undergo free radical scavenging was examined through multiple assays looking at material and cellular behavior. First, the scaffold material's ability to undergo FRS was investigated via the decomposition of hydrogen peroxide over time. It was found that both PTC10 and PTC20 scaffolds were able to significantly decrease the concentration of hydrogen peroxide at each time point over 7 days. As anticipated, PTC20 scaffolds, containing the highest amount of CNPs, experienced the largest decreases in peroxide concentration at each time point. Over 7 days, PT scaffolds showed no significant decreases in the hydrogen peroxide concentration equivalent to the control for spontaneous peroxide decomposition, confirming that the CNPs are functioning in the scaffolds. In a similar assay, Li et al. reported significant decreases in the concentration of hydrogen peroxide over 7 days after exposure to ceramic coatings containing CNPs in comparison to normal coatings without the free radical scavenging agent [38, 40]. As a final assessment, the FRS behavior of the scaffolds was assessed in a simulated in vitro study. A modified LDH assay was completed to assess cell cytotoxicity after induced oxidative stress. MC3T3 cells were exposed to media containing a 1-mM concentration of hydrogen peroxide over the span of 2 h, this time and concentration proved to provide a measurable change in cytotoxicity allowing us to quantify the effects of free radical scavenging. Cytotoxicity was then determined by quantifying LDH released from MC3T3 cells seeded on PT, PTC10, and PTC20 scaffolds. It was determined that PTC20 scaffolds were able to significantly decrease cytotoxicity in MC3T3 cells in comparison to PT scaffolds. There was no statistical significance between PTC10 scaffolds and the other scaffolds, PT and PTC20, due to the increase variance for the PTC10 sample set. Due to the increased peroxide decomposition with PTC20 shown in the previous study, it was expected to see the results reciprocated in an in vitro study. These results are supported by the work from Li et al. who reported similar protective behaviors in ceramic coatings containing CNP [38, 40].

Conclusion

It can be concluded that a nanocomposite scaffold composed of poly (1,8 octanediol-co-citrate), β-tricalcium phosphate, and cerium oxide nanoparticles can successfully support the growth of osteogenic cells and reduce the effects of oxidative stress on the cells. These inherent scaffold properties are crucial during bone tissue regeneration in areas of increased oxidative stress, such as fracture sites. Effective incorporation and function of CNPs in the polymer matrix were assessed through characterization of chemical and functional properties. CNPs were identified throughout the scaffold's porous network and were able to significantly decrease the concentration and cytotoxicity caused by hydrogen peroxide. Scaffolds containing CNPs were able to host prolific cell attachment and were confirmed to be non-cytotoxic. It can be concluded that the addition of cerium oxide nanoparticles into nanocomposite scaffolds can provide beneficial free radical scavenging behavior toward the regeneration of bone tissue. In future works, the investigation of free radical scavenging systems will expand to further assess various designs in scaffold composition and their properties. We plan to also investigate the in vitro interactions with primary human osteoblast cells, including effects on mineralization. We aim to investigate the scaffold function in in vivo animal models to study the amount of reactive oxygen species, foreign body response, mineralization, and eventually regeneration of critically sized defects. The beneficial properties of this scaffold and nanoparticles are not limited to use in bone regeneration applications and may show promise in other areas exposed to high amounts of oxidative stress, such as vascular tissue regeneration.

Acknowledgments

The authors would like to acknowledge Dr. Nancy Ruzycki and the University of Florida's Materials Science and Engineering undergraduate laboratories for use of their characterization equipment.

References

1. Liu Y, Lim J, Teoh S-H. Review: development of clinically relevant scaffolds for vascularised bone tissue engineering. Biotechnol Adv. 2013;31:688–705.
2. Andric T, Taylor BL, Whittington AR, Freeman JW. Fabrication and characterization of three-dimensional electrospun scaffolds for bone tissue engineering. Regen Eng Transl Med. 2015;1:32–41.
3. Baler K, Ball JP, Cankova Z, Hoshi RA, Ameer GA, Allen JB. Advanced nanocomposites for bone regeneration. Biomater Sci. 2014;2:1355.
4. Hutmacher DW, Schantz JT, Lam CXF, Tan KC, Lim TC. State of the art and future directions of scaffold-based bone engineering from a biomaterials perspective. J Tissue Eng Regen Med. 2007;1:245–60.
5. Scaffaro R, Lopresti F, Botta L, Rigogliuso S, Ghersi G. Preparation of three-layered porous PLA/PEG scaffold: relationship between morphology, mechanical behavior and cell permeability. J Mech Behav Biomed Mater. 2016;54:8–20.
6. Symons MCR. Radicals generated by bone cutting and fracture. Free Radic Biol Med. 1996;20:831–5.
7. Wauquier F, Leotoing L, Coxam V, Guicheux J, Wittrant Y. Oxidative stress in bone remodelling and disease. Trends Mol Med. 2009;15:468–77.
8. Karakoti AS, Monteiro-Riviere NA, Aggarwal R, Davis JP, Narayan RJ, Self WT, et al. Nanoceria as antioxidant: synthesis and biomedical applications. JOM. 2008;60:33–7.
9. Sheweita SA, Khoshhal KI. Calcium metabolism and oxidative stress in bone fractures: role of antioxidants. Curr Drug Metab. 2007;8:519–25.
10. Mandoli C, Pagliari F, Pagliari S, Forte G, Di Nardo P, Licoccia S, et al. Stem cell aligned growth induced by CeO2 nanoparticles in PLGA scaffolds with improved bioactivity for regenerative medicine. Adv Funct Mater. 2010;20:1617–24.
11. Ball JP, Mound BA, Monsalve AG, Nino JC, Allen JB. Biocompatibility evaluation of porous ceria foams for orthopedic tissue engineering. J Biomed Mater Res A. 2015;103:8–15.
12. Das S, Dowding JM, Klump KE, McGinnis JF, Self W, Seal S. Cerium oxide nanoparticles: applications and prospects in nanomedicine. Nanomedicine. 2013;8:1483–508.
13. Chigurupati S, Mughal MR, Okun E, Das S, Kumar A, McCaffery M, et al. Effects of cerium oxide nanoparticles on the growth of keratinocytes, fibroblasts and vascular endothelial cells in cutaneous wound healing. Biomaterials. 2013;34:2194–201.
14. Das S, Singh S, Dowding JM, Oommen S, Kumar A, Sayle TXT, et al. The induction of angiogenesis by cerium oxide nanoparticles through the modulation of oxygen in intracellular environments. Biomaterials. 2012;33:7746–55.
15. Karakoti A, Singh S, Dowding JM, Seal S, Self WT. Redox-active radical scavenging nanomaterials. Chem Soc Rev. 2010;39:4422–32.
16. Zhou G, Zheng B, Wei H, Zhang J, Wang S, Li Y, et al. Cerium oxide nanoparticles protect primary osteoblasts against hydrogen peroxide induced oxidative damage. Micro Nano Lett. 2014;9:91–6.
17. Karakoti AS, Tsigkou O, Yue S, Lee PD, Stevens MM, Jones JR, et al. Rare earth oxides as nanoadditives in 3-D nanocomposite scaffolds for bone regeneration. J Mater Chem. 2010;20:8912.
18. Das S, Chigurupati S, Dowding J, Munusamy P, Baer DR, McGinnis JF, et al. Therapeutic potential of nanoceria in regenerative medicine. MRS Bull. 2014;39:976–83.
19. Xu C, Qu X. Cerium oxide nanoparticle: a remarkably versatile rare earth nanomaterial for biological applications. NPG Asia Mater. 2014;6:e90.
20. Korsvik C, Patil S, Seal S, Self WT (2007) Superoxide dismutase mimetic properties exhibited by vacancy engineered ceria nanopsarticles. Chem Commun 1056.
21. Pirmohamed T, Dowding JM, Singh S, Wasserman B, Heckert E, Karakoti AS, et al. Nanoceria exhibit redox state-dependent catalase mimetic activity. Chem Commun. 2010;46:2736–8.
22. Heckert EG, Karakoti AS, Seal S, Self WT. The role of cerium redox state in the SOD mimetic activity of nanoceria. Biomaterials. 2008;29:2705–9.
23. Xiang J, Li J, He J, Tang X, Dou C, Cao Z, et al. Cerium oxide nanoparticle modified scaffold interface enhances vascularization of bone grafts by activating calcium channel of mesenchymal stem cells. ACS Appl Mater Interfaces. 2016;8:4489–99.

24. Thadavirul N, Pavasant P, Supaphol P. Development of polycaprolactone porous scaffolds by combining solvent casting, particulate leaching, and polymer leaching techniques for bone tissue engineering. J Biomed Mater Res A. 2014;102:3379–92.
25. Kothapalli CR, Shaw MT, Wei M. Biodegradable HA-PLA 3-D porous scaffolds: effect of nano-sized filler content on scaffold properties. Acta Biomater. 2005;1:653–62.
26. Roohani-Esfahani S-I, Nouri-Khorasani S, Lu Z, Appleyard R, Zreiqat H. The influence hydroxyapatite nanoparticle shape and size on the properties of biphasic calcium phosphate scaffolds coated with hydroxyapatite–PCL composites. Biomaterials. 2010;31:5498–509.
27. Lobo SE, Livingston Arinzeh T. Biphasic calcium phosphate ceramics for bone regeneration and tissue engineering applications. Materials (Basel). 2010;3:815–26.
28. Erisken C, Kalyon DM, Wang H. Functionally graded electrospun polycaprolactone and β-tricalcium phosphate nanocomposites for tissue engineering applications. Biomaterials. 2008;29:4065–73.
29. Rezwan K, Chen QZ, Blaker JJ, Boccaccini AR. Biodegradable and bioactive porous polymer/inorganic composite scaffolds for bone tissue engineering. Biomaterials. 2006;27:3413–31.
30. Leong K, Chua C, Sudarmadji N, Yeong W. Engineering functionally graded tissue engineering scaffolds. J Mech Behav Biomed Mater. 2008;1:140–52.
31. Rogel MR, Qiu H, Ameer GA. The role of nanocomposites in bone regeneration. J Mater Chem. 2008;18:4233.
32. Begam H, Nandi SK, Kundu B, Chanda A. Strategies for delivering bone morphogenetic protein for bone healing. Mater Sci Eng C. 2017;70:856–69.
33. Yang J, Webb AR, Pickerill SJ, Hageman G, Ameer GA. Synthesis and evaluation of poly(diol citrate) biodegradable elastomers. Biomaterials. 2006;27:1889–98.
34. Tavares DS, Castro LO, Soares GDA, Alves GG, Granjeiro JM. Synthesis and cytotoxicity evaluation of granualar magnesium substituted I2 tricalcium phosphate. J Appl Oral Sci. 2013;21:37–42.
35. Liu YH, Zuo JC, Ren XF, Yong L. Synthesis and character of cerium oxide (CeO2) nanoparticles by the precipitation method. Metalurgija. 2014;53:463–5.
36. Allo BA, Costa DO, Dixon SJ, Mequanint K, Rizkalla AS. Bioactive and biodegradable nanocomposites and hybrid biomaterials for bone regeneration. J Funct Biomater. 2012;3:432–63.
37. Mody N, Parhami F, Sarafian TA, Demer LL. Oxidative stress modulates osteoblastic differentiation of vascular and bone cells. Free Radic Biol Med. 2001;31:509–19.
38. Li K, Xie Y, You M, Huang L, Zheng X. Cerium oxide-incorporated calcium silicate coating protects MC3T3-E1 osteoblastic cells from H2O2-induced oxidative stress. Biol Trace Elem Res. 2016;174:198–207.
39. Habraken W, Habibovic P, Epple M, Bohner M. Calcium phosphates in biomedical applications: materials for the future? Mater Today. 2016;19:69–87.
40. Li K, Xie Y, You M, Huang L, Zheng X. Plasma sprayed cerium oxide coating inhibits H2O2-induced oxidative stress and supports cell viability. J Mater Sci Mater Med. 2016;27:100.